A 3D pantographic metamaterial behaving as a mechanical shield: Experimental and numerical evidence

Alessandro Ciallella, Ivan Giorgio, Emilio Barchiesi, Gianluca Alaimo, Alberto Cattenone, Benjamin Smaniotto, Antoine Vintache, Francesco d'Annibale, Francesco Dell'Isola, François Hild, et al.

A 3D pantographic metamaterial behaving as a mechanical shield: Experimental and numerical evidence

Alessandro Ciallella[1,2], Ivan Giorgio[1,2], Emilio Barchiesi[3,2], Gianluca Alaimo[4], Alberto Cattenone[4], Benjamin Smaniotto[5], Antoine Vintache[5], Francesco D'Annibale[1,2], Francesco dell'Isola[1,2,5,6], François Hild[5], and Ferdinando Auricchio[4,7]

[1]Department of Civil, Construction-Architectural and Environmental Engineering (DICEAA), University of L'Aquila, L'Aquila, Italy

[2]International Research Center for the Mathematics and Mechanics of Complex Systems (M&MoCS), University of L'Aquila, L'Aquila, Italy

[3]Architecture, design and urban planning (DADU), University of Sassari, Alghero, Italy

[4]Department of Civil Engineering and Architecture (DICAr), University of Pavia, Italy

[5]Université Paris-Saclay, CentraleSupélec, ENS Paris-Saclay, CNRS LMPS–Laboratoire de Mécanique Paris-Saclay, Gif-sur-Yvette, France

[6]Faculty of Mechanical and Industrial Engineering, Warsaw University of Technology, Warsaw, 02-524, Poland

[7]Research Associate at IMATI-CNR Pavia, Italy

December 29, 2023

Abstract

Multilayer pantographic metamaterials, in short, pantographic blocks, have shown peculiar mechanical behavior, especially when their constitutive hinges are revolving (*i.e.,* perfect) joints. The pantographic block, which is the subject of the present paper, has been printed using a Powder Bed Fusion technology and its hinges may be modeled as perfect ones. In the reported *in situ* 3-point flexural test, the predictions obtained by second gradient models for its mechanical response are shown to be experimentally consistent thanks to measurements via Digital Volume Correlation. The deformation applied by the upper central support is almost entirely shielded by the pantographic block, namely, the specimen barely crosses through the reference bottom plane defined by the lower lateral supports, even when subjected to very large

deformations. The mathematical model employed herein captures this observation in terms of a nonlinear 'arching' effect activated in the beams of the pantographic structure, provided elastic locking is introduced to prevent pantographic zero-energy modes.

Keywords: Digital Volume Correlation (DVC), Metamaterials, Pantographic block, Second Gradient Continua, Generalized continua.

1 Introduction

A mechanical metamaterial is a material designed to have unique mechanical properties that are uncommon in standard materials. It is a class of materials that are designed with the aim of tailoring their mechanical response [10, 27, 6, 2, 3, 1, 52, 15, 57]. Such metamaterials achieve their properties through carefully engineered internal structures or geometries rather than relying solely on the properties of the constituents. These internal structures may exhibit unusual mechanical behavior, such as negative Poisson's ratio (auxetic behavior) [55, 26, 67, 66, 42, 43], negative elastic modulus [25, 39], high mechanical damping [46, 35, 14], wide elastic domain [17, 34, 36, 47, 32], or high toughness and strength [60, 40, 13, 28, 74]. By precisely designing the shape, arrangement, and size of the internal architecture (*i.e.,* structural elements), mechanical metamaterials may exhibit properties that are not seen in conventional materials. For example, they possess extreme stiffness or flexibility, exceptional energy absorption or dissipation capabilities, or unique wave propagation characteristics. Some metamaterials can have their properties even programmed or tuned (see, e.g., [50, 51] where shape memory composites are employed or [29]). Possible applications of mechanical metamaterials are broad and include areas such as vibration damping, impact protection, acoustic insulation, and advanced structural engineering. They hold promises for creating materials with superior performance in various industries, including aerospace, automotive, civil engineering, and consumer electronics.

A pantographic structure is a specific type of metamaterial design that is inspired by the mechanical properties of pantographs or scissor mechanisms [18]. It consists of two interconnected families of long structural elements that are connected by flexible or rotating joints, see Figure 1. These joints allow the structure to deform in a prescribed manner when subjected to external forces because of the pantographic mechanism.

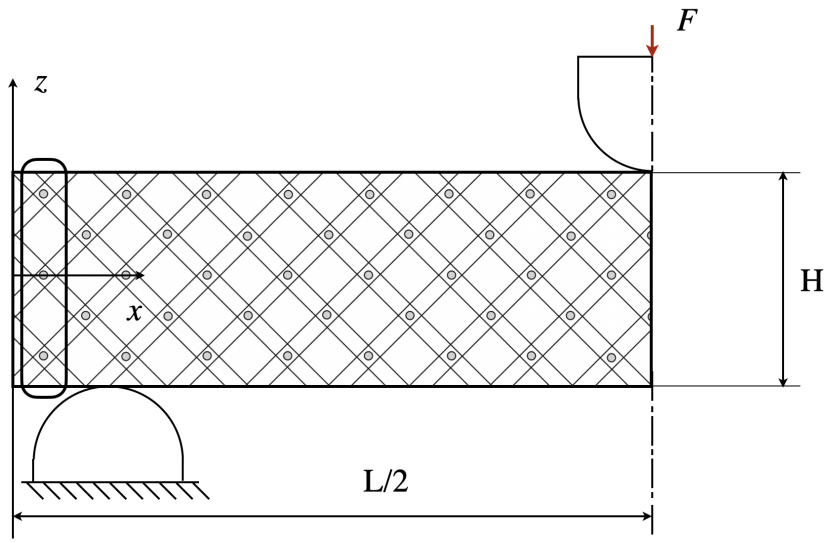

Figure 1: Schematic representation of a half sample of a symmetric pantographic structure subjected to 3-point flexure. On the left of the sample, a constraining device is added to avoid zero-energy modes.

Pantographic structures exhibit several specific mechanical features, such as applying a local deformation to a specific location causes the occurrence of a significant deformation far away from the source point, which also entails a wide range of elastic behavior for this metamaterial. From a modeling viewpoint, this type of architecture is characterized by a second gradient energy in the continuum description [4, 63]. The first prototypes of such metamaterial were proposed as bidimensional sheets. Herein, a generalization multilayered three-dimensional structure is studied. Its connections are made of joints that allow for the construction of a stack of pantographic sheets (Figure 2).

Pantographic metamaterials owe the majority of their mechanical properties to the fact that they belong to the class of deployable structures. Such a class includes notable structures such as origami [69], solar panels for spacecraft, umbrellas, vascular stents, scissor lifts, and expanding barriers, just to name a few. They all share the property that they can reconfigure and change shape/size, mainly from folding and unfolding at the cost of zero or nearly-zero deformation energy. From the mathematical point of view, deployability, which is the most representative feature of pantographic metamaterials, implies challenges, too. Deployability means that the pattern geometry can deploy and collapse with no associated deformation energy, which, at the continuum scale, induces that the deformation energy is non-coercive. A more detailed mathematical formulation is thus needed [23, 24].

Unless one is interested in the admissible kinematics rather than in the load-bearing capacity of pantographic metamaterials (with an associated nonlinear structural response), the zero-energy modes at the global level should be avoided (*i.e.,* locked) both in continuum and discrete descriptions (and, of course, in experiments, as it was done in that reported in the present contribution) by applying suitable boundary con-

ditions or by introducing in the structure mechanical devices (specified in an energetic approach by means of an elastic potential), such as springs that avoid the zero-energy non-rigid deformation modes. In the present contribution, the rigid (zero-energy) motions were avoided by applying suitable boundary conditions, namely, printing four structural elements that constrained the four short sides of the pantographic mechanism.

It is worth mentioning that the working mechanism of pantographic metamaterials may be exploited at different scales to obtain extremely exotic and complex behaviors. In the simplest case, when the pantographic motif is repeated periodically at just one single scale (for more complex multiscale geometrical arrangements making use of the pantographic motif, see Refs. [7, 8]), such a mechanism confers to pantographic metamaterials extremely high compliance to loading (globally, but especially far from constrained regions), at least when the fibers constituting the metamaterial do not get into contact. In a bias extension test [18], as the applied load increases, fiber flexure increases at quasi-rigid-to-deformed region transition zones. When contact occurs and shear deformation cannot increase anymore (at an extremely convenient cost of deformation energy) to comply with external boundary conditions without fiber stretching, as it happens in regions far from clamps, fiber stretching together with fiber flexure make the deformation energy increment increase dramatically as loading increases. This last phenomenon is the so-called stiffening phase of pantographic fabrics that, together with the compliant phase observed at the beginning of the test, characterizes the nonlinear elastic response of pantographic metamaterials. For different (global) loading conditions, like those applied in the three-point flexural test considered herein, similar deformation patterns and structural responses are observed [70, 71, 56], if local or global buckling does not occur [9, 62].

The peculiarity of the considered pantographic block lies in the fact that the joints among the structural elements that compose it revolve, which allow relative rotational motions between the connected beams. This construction makes the shear stress negligible, which is replaced by a second-gradient hyperstress originating from beam flexure. Therefore, the stress inside the block undergoes a redistribution that alters the mechanical response of the specimen in an uncommon way and provides a shield capacity from a possible applied load. This stress redistribution inside the sample is similar to the arching effect observed in certain geotechnical engineering scenarios [54, 48, 11]. The arching effect in soils is a phenomenon where the soil pressure is redistributed due to relative motion between its adjoining portions. This phenomenon commonly occurs when the soil interacts with structural elements, such as tunnels, retaining walls, buried structures, and piles in pile-supported embankments. This effect is caused by the shear stress, which arises within the soil. When the ground is subjected to a load, it will want to deform. However, the shear stress occurring in the soil, in addition to the hydrostatic stress, will partially prevent this deformation, thereby improving its load-bearing capacity. This resistance to deformation will cause the soil to arch over the yielding portion of the support. The arching effect is notable in geotechnical engineering because it reduces the load on structures. For example, in a pile-supported embankment, the arching effect reduces the load on the piles by redistributing

the load to the surrounding soil. This mechanism helps to reduce the cost of the embankment and makes it more stable [58].

It was highlighted, both numerically and experimentally, that pantographic metamaterials have an exotic behavior that can be exploited to diffuse the deformation energy induced in the specimens even by highly concentrated external loads [19, 20]. In this paper, a possible elastic locking of pantographic floppy modes is discussed, which allows for the efficient distribution of the deformation energy inside a pantographic block undergoing three-point flexure. The beams constituting the pantographic structure are deformed in a flexural mode, which globally involves all the cells of the mesostructure. An arch effect, in the inverse direction with respect to the applied load, may be activated, which becomes more and more relevant in the regime of large deformation. The pattern of bent beams, which is observed in the deformation process, is suggestive and shows nonlocality, thereby allowing for the shielding effect of the lower face of the block, which remains essentially undeformed even when the upper support penetrates the specimen.

The possibility of describing the specimen under study with a continuous three-dimensional model is also investigated. Specifically, the continuum modeling of the pantographic block follows the approach of Stilz et al. [65]. The interest, besides the conceptual one in assessing the possible limitations of the model in predicting the behavior of the object of study, is in overcoming in the future the difficulty of implementing sufficiently accurate initialization in the algorithm measuring displacement fields by Digital Volume Correlation (DVC), following the model-driven initialization procedure presented in Ref. [12]. This approach is considered highly relevant to deal with cases with large displacements, especially for mesostructured objects where the repeated unit cells give rise to a period structure that easily traps DVC analyses in local minima, making correct measurements very challenging, if even possible. The outline of the paper is as follows. In Section 2, the nominal geometry of the specimen and the description of the fabrication procedure are presented. Section 3 is devoted to the introduction of the continuous model considered herein. In Section 4, the 3-point flexural experiment with the DVC measurement procedure is illustrated. The results of numerical simulations are introduced and compared with experimental analyses.

2 Geometry and 3D printing process

2.1 Nominal geometry

The design of the pantographic block studied hereafter is shown in Figure 2. The nominal geometry is that of a rectangular cuboid with sides 192.9 mm, 88.7 mm and 52.2 mm, where the dimension of the pantographic plane is 192.9×52.2 mm^2, while in the direction parallel to the cylindrical shafts acting as pivots the sample length is 88.7 mm. In Figure 2, the pantographic plane is illustrated by the front view, where one refers to the long side direction as the longitudinal direction and the short one as the vertical direction. In the top and

side views, the transverse direction is plotted versus the longitudinal and the vertical ones, respectively. The shadowing of the 3D rendering in Figure 2 allows the distances from the observation point of the different elements of the structure to be perceived. The longitudinal, transverse, and vertical directions are associated with the axes $\{x\}$, $\{y\}$, and $\{z\}$, respectively. Hence, in the nominal configuration, the planes $\{x, z\}$ contain the beams of the pantographic mechanism, while the shafts acting as pins in the hinges are parallel to $\{y\}$. The structure is designed to have 8 layers of beams associated with pantographic sheets, where the connection between two successive layers is made of 38 hinges (*i.e.,* 8 vertical rows of 3 hinges alternating with 7 rows of 2 hinges, Figure 2). The beams have a rectangular cross-section of 4.5×2 mm^2, and the connecting shafts are cylinders 4 mm in diameter, which restrict to 2 mm where, intersecting the beams, the cylinder acts as a pin (Figure 2). To mimic the sleeve in the bars, circular holes are present with a gap with the shaft allowing for a perfect hinge behavior. The pitch between the centers of two successive holes on the beams is 16 mm, while in the $\{y\}$ direction parallel to the shaft, the spacing between two successive beams is 9 mm.

The geometric parameters were meticulously selected to optimize the 3D printing process of the pantographic metamaterial. Such a task is challenging, but through careful considerations, the parameters were selected to ensure the highest possible quality of the manufacturing process, while prescribing the maximum size of samples to be examined via computed tomography.

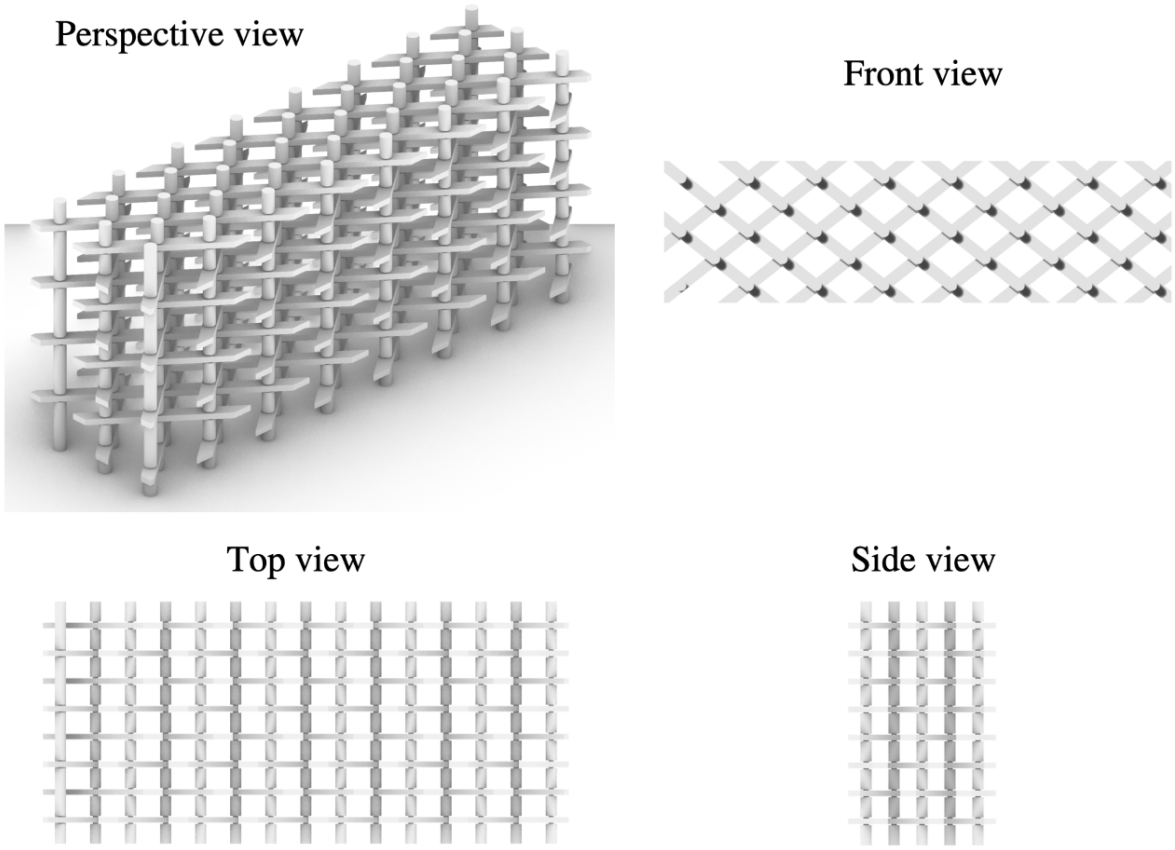

Figure 2: Renderings of the nominal geometry of the considered pantographic block.

2.2 Specimen fabrication

Starting from the nominal geometry illustrated in Section 2.1, the pantographic block under investigation was manufactured with a polyamide 12 (PA12) polymer processed by an HP 580 MultiJet Fusion 3D printer available at the ProtoLab 3D-printing laboratory of the University of Pavia. Such an additive manufacturing system is powder-bed-based, where the power source for melting the feedstock is an electric lamp. The virtual model (CAD or mesh) of the part to be manufactured is first sliced into layers, which are subsequently processed by the printing software to obtain all the necessary data to be sent to the 3D printer. The process starts with the deployment of a 0.1 mm thick powder layer. It continues with the printing head that selectively deposits a fusing agent in the internal part of the sections to be molten and a detailing agent at the interface between the sections and the surrounding powder. Last, the electric lamp moves on the top of the layer, transferring heat to the powder by thermal irradiation. All these sub-steps are repeated for each 0.1-mm thick layer until the part is completed. The fusing agent deposited in the internal part of the section increases the powder thermal conductivity, thus allowing for complete and fast melting inside the section to be built. The detailing agent deposited at the interface between the sections and the surrounding powder decreases the powder thermal conductivity allowing it to obtain enhanced dimensional accuracy at the section boundaries.

One of the most remarkable characteristics of the HP MultiJet manufacturing process is that it is a support-free technology. Thanks to this feature, there are two main advantages, namely, i) the only post-processing needed is mere sandblasting to remove the unmolten powder that remains attached to the outer surfaces of the part, and ii) pins can be oriented vertically (*i.e.,* along the printing direction), thereby allowing for the best pantograph orientation with respect to geometrical accuracy inside the building volume. Despite these advantages, the design of the pantograph remains critical because great care must be paid to the sizing of the clearances between all the parts. The main challenge in pantograph fabrication is making the pin-beam connections with as little gap as possible with no locking. Both axial and radial clearances (Figure 3) were selected accordingly.

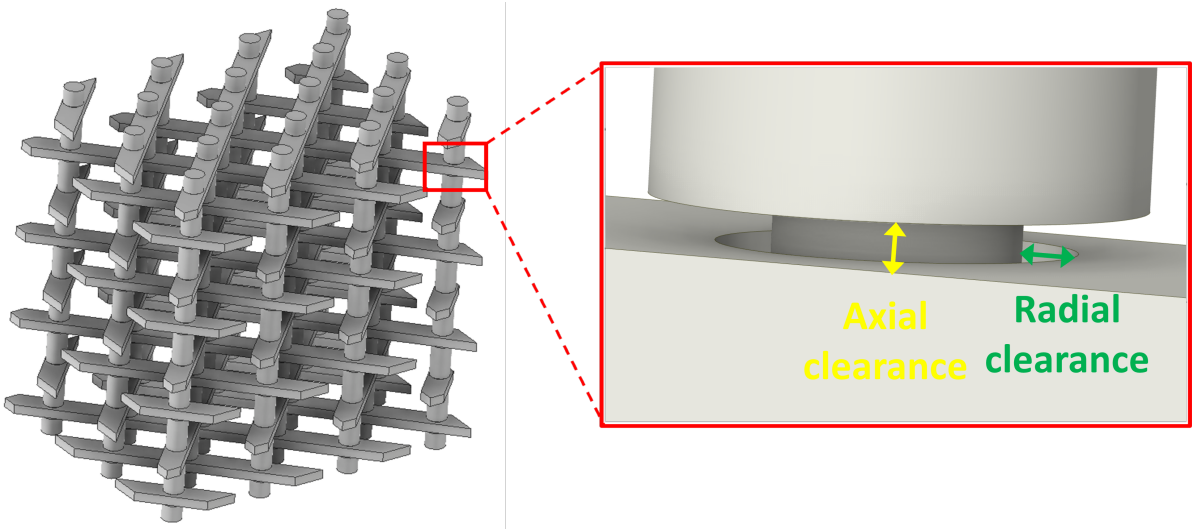

Figure 3: Axial and radial gaps.

To obtain optimal clearances, a design of experiment approach was utilized, which generated a set of design points resulting from the combination of different axial and radial backslashes. Relying on past experience, the possible combinations were limited to those reported in Table 1. Each design point was studied by producing a small portion of the pantograph characterized by the corresponding values of axial and radial clearances. The functionality of each design point was evaluated after sandblasting and a series of training cycles to obtain the required relative motions. The pin-sleeve connection should not become loose when the specimen is subjected to loads and, at the same time, must ensure the relative motions of the hinge. Therefore, a compromise was made to provide the relative rotation at each joint without introducing other spurious degrees of freedom. The best solution was *Design point 5*, which corresponds to an axial clearance of 0.40 mm, and a radial clearance of 0.15 mm.

Table 1: Design points for evaluating optimal axial and radial clearances (point 5)

Design point	Axial clearance mm	Radial clearance mm
1	0.35	0.10
2	0.35	0.15
3	0.35	0.20
4	0.40	0.10
5	**0.40**	**0.15**
6	0.40	0.20
7	0.45	0.10
8	0.45	0.15
9	0.45	0.20

3 Strain energy of continuum model

The structure of the pantographic block presented in Section 2.1 is characterized by three dominant directions associated with the axes of a lattice made of beams. The first two determine the plane of the pantographic mechanism. In the reference configuration, the unit vectors $\mathbf{L}$ and $\mathbf{M}$ define the directions parallel to the beams lying on this plane (see Figure 4). The third unit vector $\mathbf{N}$ is introduced to describe the direction parallel to the axis of the shafts (*i.e.,* transverse direction).

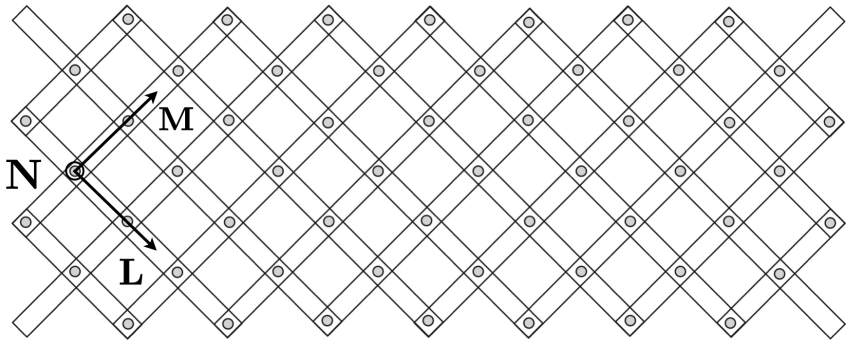

Figure 4: Main directions of the pantographic lattice in the reference configuration.

Let $\boldsymbol{F}$ denote the gradient of the placement field (*i.e.,* the standard deformation tensor), the images of these three vectors in the current (deformed) configuration are described in terms of the unit vectors $\boldsymbol{l}$, $\boldsymbol{m}$, $\boldsymbol{n}$

$$\lambda\,\boldsymbol{l} = \boldsymbol{F}\mathbf{L}, \quad \mu\,\boldsymbol{m} = \boldsymbol{F}\mathbf{M}, \quad \eta\,\boldsymbol{n} = \boldsymbol{F}\mathbf{N} \tag{1}$$

where $\lambda = \|\boldsymbol{F}\mathbf{L}\|$, $\mu = \|\boldsymbol{F}\mathbf{M}\|$, and $\eta = \|\boldsymbol{F}\mathbf{N}\|$. Denoting by π the plane parallel to the directions $\mathbf{L}$ and $\mathbf{M}$, and since it is assumed that in the transverse direction all these planes behave in the same way (*i.e.,* homogeneity of the pantographic sheets in the transverse direction). Following the approach of Stilz et al. [65], the strain energy density for any plane parallel to π reads

$$\begin{aligned} w_\pi = \frac{1}{2}\big\{ &\mathrm{K}_e[(\lambda-1)^2 + (\mu-1)^2] + \mathrm{K}_t\ (\kappa_{tL}^2 + \kappa_{tM}^2) + \\ &\mathrm{K}_n\ (\kappa_{nL}^2 + \kappa_{nM}^2) + \mathrm{K}_g\ (\kappa_{gL}^2 + \kappa_{gM}^2)\big\} \end{aligned} \tag{2}$$

where the constants K_e, K_t, K_n, K_g, K_{eN}, K_{sN}, and K_c are (meta)material-dependent parameters. In Equation (2), there are two kinds of contributions. The first two terms are related to first-gradients of the displacement. They take into account the measures of deformation $(\lambda-1)$, and $(\mu-1)$, describing the change of length in the directions $\mathbf{L}$ and $\mathbf{M}$. In principle, one should also consider a contribution related to the

change of angle between the directions parallel to the beams constituting the pantographic lattice from the reference to the current configuration. However, since the aim is to model the presence of perfect hinges, this contribution is negligible. The remaining terms of Equation (2) are instead second-gradient contributions. They take into account the energy associated with measures of deformation representing twist and curvature in directions **L** and **M**, respectively. In particular, the measures of twist deformation, flexure normal to the plane π, and geodesic flexure are introduced [65]

$$\kappa_{tL} = (\boldsymbol{n} \times \boldsymbol{l}) \cdot \frac{\mathrm{d}\boldsymbol{n}}{\mathrm{d}S_L} \quad , \quad \kappa_{nL} = \boldsymbol{n} \cdot \frac{\mathrm{d}\boldsymbol{l}}{\mathrm{d}S_L} \quad , \quad \kappa_{gL} = -(\boldsymbol{n} \times \boldsymbol{l}) \cdot \frac{\mathrm{d}\boldsymbol{l}}{\mathrm{d}S_L} \tag{3}$$

and

$$\kappa_{tM} = (\boldsymbol{n} \times \boldsymbol{m}) \cdot \frac{\mathrm{d}\boldsymbol{n}}{\mathrm{d}S_M} \quad , \quad \kappa_{nM} = \boldsymbol{n} \cdot \frac{\mathrm{d}\boldsymbol{m}}{\mathrm{d}S_M} \quad , \quad \kappa_{gM} = -(\boldsymbol{n} \times \boldsymbol{m}) \cdot \frac{\mathrm{d}\boldsymbol{m}}{\mathrm{d}S_M} \tag{4}$$

for directions **L** and **M**, respectively. In Equations (3) and (4), S_L and S_M are the abscissas along the two beam directions. The energy density (2) is based on a Kirchhoff beam model [30, 37, 38].

In **N** direction of the shafts, only a first-gradient contribution is considered

$$w_N = \frac{1}{2}\left\{\mathrm{K}_{eN}(\eta-1)^2 + \mathrm{K}_{sN}(\gamma_{LN}^2 + \gamma_{MN}^2) + 2\,\mathrm{K}_c\left[(\lambda-1)(\eta-1) + (\mu-1)(\eta-1)\right]\right\} \tag{5}$$

The first term represents the elastic energy associated with the change of length in direction **N**, while the second contribution takes into account shear in directions **L** and **N** as well as **M** and **N**. The shear strains are defined by

$$\sin\gamma_{LN} = \boldsymbol{l} \cdot \boldsymbol{n}, \quad \sin\gamma_{MN} = \boldsymbol{m} \cdot \boldsymbol{n} \tag{6}$$

The last term accounts for an exchange of energy between stretching modes in the pantographic plane π and the orthogonal direction **N**.

4 Experimental evidence and numerical simulations

4.1 Experimental setup and elastic locking

The printed specimen was subjected to an *in situ* 3-point flexural test performed in the X50+ North Star Imaging tomograph of LMPS. The displacement of the upper support was prescribed with the miniTTC (Deben) testing machine in the pantographic plane (*i.e.,* parallel to the vertical $\{z\}$-axis). Four beams whose cross-sectional area was 7.9×3.6 mm^2 were employed as elastic locking to constrain the possible configurations to avoid zero-energy (floppy) modes. The beams were printed with the same procedure as the pantographic block and designed to have three circular holes where the cylinder ends were constrained at a distance of 20 mm between the centers of two successive ones. To achieve locking, the last left and right vertical rows of

cylindrical shafts of the sample were inserted into these beams (Figure 5).

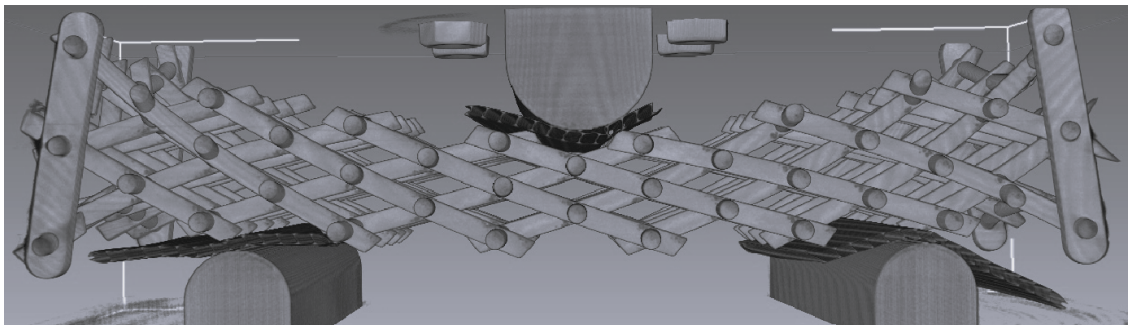

Figure 5: 3D rendering of the reconstructed volume corresponding to a 28 mm prescribed displacement to the upper support. The two lateral locking beams are visible.

During the experiment, three-dimensional scans of the specimen were acquired via micro-computed X-ray tomography [53], in the reference configuration and in the loaded states. Figure 5 also shows the supports, which are mounted on the lower and upper platens of the *in situ* testing machine. On the bottom platen, two supports with semicircular ends were fixed at a distance of 130 mm, while one support was placed in the middle position with respect to both of them. They were made of ABS by Fused Deposition Modeling (FDM). The upper platen was steady during the test, and the motion of the lower platen was applied until the maximum stroke allowed by the testing machine was reached. Corrugated cardboard (*i.e.,* undulated polypropylene sheet) was inserted between the sample and the supports to keep the ends of the beams from locking against them.

The sample was scanned several times during the test. First, two scans were acquired in the unloaded configuration after placing the specimen in the testing machine, ready to start the experiment. The first one was considered as the reference (*i.e.,* scan of the reference configuration) while the second was used to estimate measurement uncertainties and the baseline levels for correlation residuals. In the loaded configurations, with progressively increased prescribed stroke, six additional scans were acquired (numbering from 1 to 6). Scan # 1 was acquired after 8 mm prescribed stroke. The other five scans were acquired every 4 mm so that the stroke was 12, 16, 20, 24, and 28 mm for scans #2 to #6. The hardware parameters of the test are reported in Table 3. The reconstructed volumes correspond to $240 \times 99.3 \times 74.9$ mm^3 with a 116 µm / vx resolution (corresponding to $2069 \times 856 \times 646$ voxels). In Figure 5, the reconstructed volume corresponds to the maximum prescribed stroke.

The reaction force vs. prescribed displacement measured during the experiment is shown in Figure 6. The force was recorded during the loading steps. The seven vertical black bars correspond to force measurements during tomographic scans at a fixed stroke. A small softening is observed for large strokes. However, no significant plasticity and/or damage phenomena appeared during the test. After unloading at the end of the test, a visual inspection showed no significant permanent deformation or damage. It is important to note

that repeated loading/unloading cycles may cause plasticity and/or damage to occur. Although it has not been investigated so far, it is important to explore this aspect in future research.

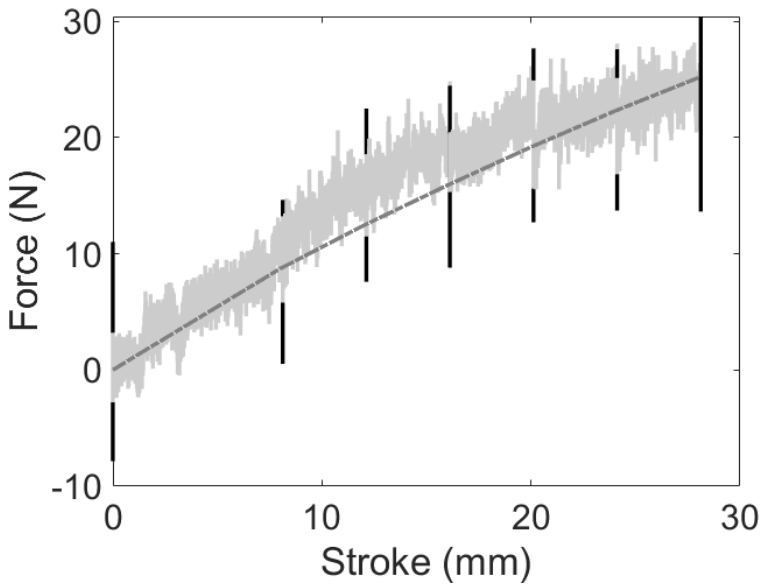

Figure 6: Comparison between force vs. stroke measured during the test (vertical black bars and light gray), and simulated via FE simulations (dash-dotted dark gray line).

4.2 Parameter Calibration

A heuristic calibration of the model parameters was performed to fit the force vs. stroke plot (Figure 6). The calibrated parameters used herein for the numerical simulation are reported in Table 2.

Table 2: Calibrated model parameters

K_e	2.1×10^7 N/m^2
K_g	35 J/m
K_n	7.0 J/m
K_t	5.87 J/m
K_{eN}	1.9×10^6 N/m^2
K_{sN}	2.1×10^5 N/m^2
K_c	2.4×10^6 N/m^2

4.3 DVC analysis

FE-based DVC [61, 45] was employed to produce the measurements of the described experiment. The displacement field $\mathbf{u}$ between the reference and the loaded configurations is sought in terms of $\mathbf{N_i}(\mathbf{x})$, the vectorial shape functions, associated with the nodal displacements υ_i

$$\mathbf{u}(\mathbf{x}, \{\boldsymbol{\upsilon}\}) = \sum_i \upsilon_i \mathbf{N_i}(\mathbf{x}). \tag{7}$$

where the column vector $\{\boldsymbol{v}\}$ collects the nodal displacements v_i, which are the unknowns of the analysis. To evaluate them, a minimization procedure for the sum of squared gray level differences is carried out. The gray level residual ρ is defined for any voxel belonging to the region of interest (ROI) as

$$\rho(\mathbf{x}, \{\boldsymbol{v}\}) = I_0(\mathbf{x}) - I_t(\mathbf{x} + \mathbf{u}(\mathbf{x}, \{\boldsymbol{v}\})), \tag{8}$$

where I_0 and I_t are the gray level for each voxel in the reference and deformed configurations, respectively. The DVC cost function reads

$$\Phi_c^2(\{\boldsymbol{v}\}) = \sum_{\mathbf{x} \in ROI} \rho^2(\mathbf{x}, \{\boldsymbol{v}\}), \tag{9}$$

and penalized to perform so-called Hencky-elasticity regularization [20]

$$\Phi_m^2(\{\boldsymbol{v}\}) = \{\boldsymbol{v}\}^\top [\mathbf{K}]^\top [\mathbf{K}] \{\boldsymbol{v}\} \ , \tag{10}$$

so that the measured nodal displacements via regularized DVC minimize the weighted sum

$$\{\boldsymbol{v}\}_{\text{meas}} = \arg\min_{\{\boldsymbol{v}\}} \left(\Phi_c^2(\{\boldsymbol{v}\}) + w_m \Phi_m^2(\{\partial \boldsymbol{v}\}) \right) \ , \tag{11}$$

where $\{\partial \boldsymbol{v}\}$ denotes the column vector of incremental displacements from one step in the analysis to the next, and $[\mathbf{K}]$ the rectangular stiffness matrix associated with bulk and free surface nodes. The regularization weight w_m is proportional to the so-called regularization length ℓ_m, raised to the power 4 [68].

4.3.1 Nominal to reference meshes

The model of the to-be-printed specimen (in STL format) was used to create a mesh of the specimen to focus the analysis on the regions of interest. Figure 7 shows the mesh in the nominal configuration generated with Ansys Mechanical meshing software release 2022 R1. It was made of 76,220 nodes and 245,443 4-noded tetrahedra (*i.e.,* T4 elements) whose mean size (measured as the cube root of the average elementary volume) was 6 vx. The backtracking procedure on the reconstructed volumes and the next DVC steps, illustrated below, were performed using the Correli 3.0 framework [49] in which Hencky's regularization was implemented (Table 4).

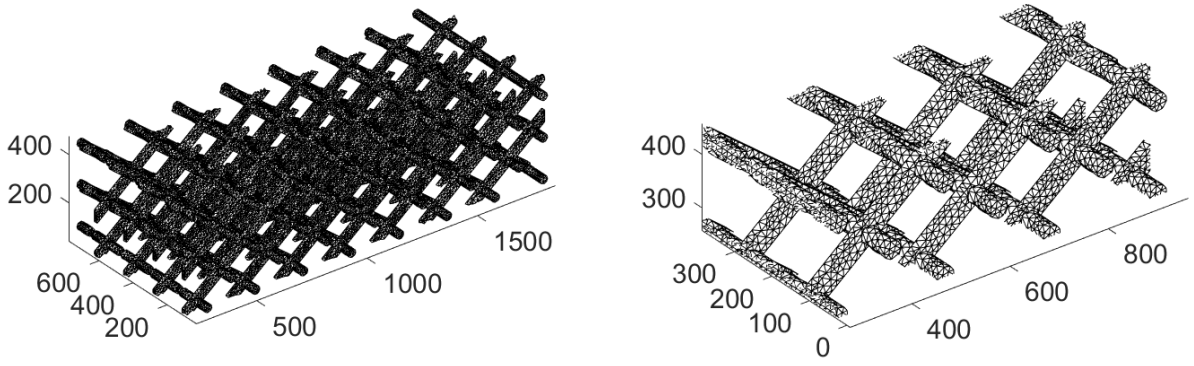

(a) (b)

Figure 7: T4 FE mesh built on the nominal configuration. (a) Overall discretization and (b) detail of the meshing. The axis labels are expressed in voxels.

The mesh is, by construction, consistent with the nominal configuration. Small printing defects, as well as possible preload and incorrect sample placement, prevent the reference (experimental) configuration from exactly matching the nominal geometry used for printing. A backtracking procedure [5] was employed to fit the mesh built from the designed geometry to the reference unloaded scan. The STL model is also required to create a voxelized digital twin of the nominal geometry by means of a ray-tracing algorithm [59]. Last, correlating the reference scan with the voxelized twin allows the displacement field between the two to be measured. The field is then used to update the position of the mesh nodes to fit on the reference scan. Regularized DVC [68] was run for this purpose, making use of a coarse auxiliary mesh encompassing the volume in the printed configuration.

Figure 8 shows the displacement field measured at the end of the backtracking procedure after removing rigid-body translations required to transport the reconstruction frame into the digital twin frame. The difference between the nominal and printed configurations is particularly pronounced in this case, especially in the longitudinal direction. The specimen had to be elongated more than $4,5$ mm overall. It took a slight U-shape visible from the vertical component of the field. The transverse direction also involved some small differences with respect to the nominal geometry. All these differences are almost entirely due to the presence of clearances between the beams and cylinders acting as hinges, which in the printed configuration were redistributed.

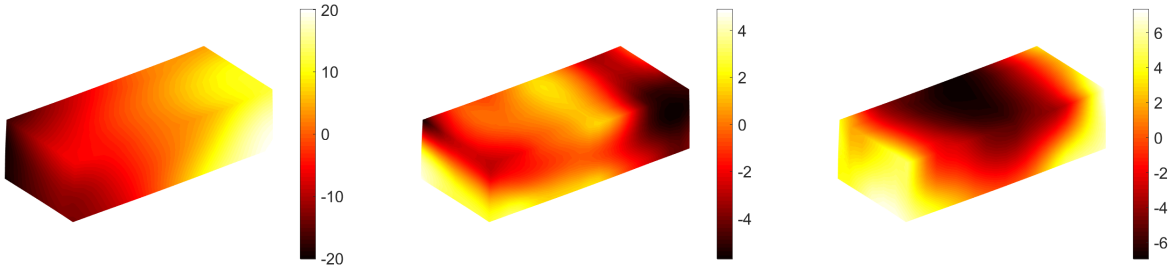

(a) (b) (c)

Figure 8: Displacement fields in the longitudinal (a), transverse (b), and vertical (c) directions obtained by the backtracking procedure. The fields are shown on the deformed configuration and expressed in voxels.

4.3.2 Direct DVC calculations

DVC analyses were run taking as reference the first undeformed scan for all the other seven scans. The presence of the perfect hinges made ineffective the use of a macroscopic (and coarse) mesh. The analyses had to be run directly with the backtracked mesh. Given the very large displacement amplitudes, the DVC calculations stopping criterion was set to an L^2-norm of displacement corrections less than 2×10^{-1} vx. This level was chosen as the same order of magnitude as the standard displacement uncertainty (for the selected regularization length) evaluated with the repeated unloaded scan (*i.e.,* $\approx 10^{-1}$ vx).

The following analyses required careful initialization to allow the DVC algorithm to converge to the absolute minimum. The low density of hinges allowed for manual initialization, whereas a model-driven initialization procedure would probably have been required for large displacements in case of a higher number of hinges [12]. For the mid-section, the hinge placements were manually clicked. Their corresponding displacement could then be obtained. These displacements were applied to each hinge element, which were the master nodes. All other (*i.e.,* slave) nodal displacements were determined by using Guyan reduction [41]. The displacements in the transverse direction were assumed to be uniform. With such initialization, it was possible to converge. The fluctuations of gray-level RMS residuals in the various scans were mostly related to the different positioning of the ends of the beams with respect to the cardboard and to the presence of the locking beams acting as constraints (Figure 9).

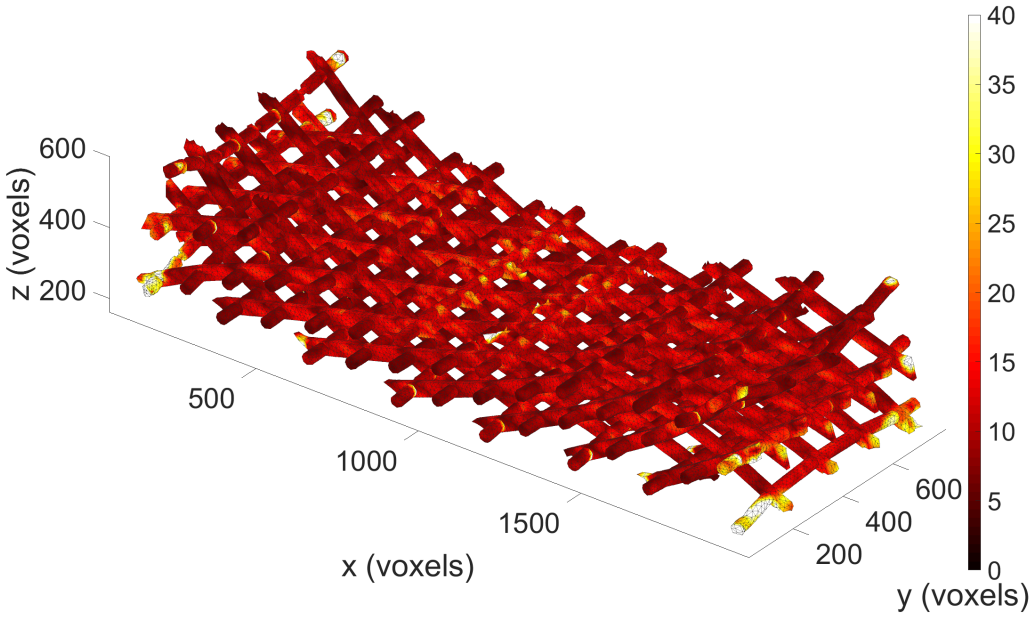

Figure 9: Gray level residuals on the mesh in its deformed configuration for the maximum prescribed deflection (*i.e.,* 28 mm stroke). Axis labels are expressed in voxels. The reconstructed volumes have a dynamic range of 255 gray levels (*i.e.,* 8-bit digitization).

To select the regularization length, different DVC analyses were run by gradually reducing ℓ_m. Figure 10(a) shows the root mean square (RMS) gray level residual Φ_c for the undeformed repeated scan (Scan # 0) and all loaded ones (Scan # 1 to 6, respectively) for different regularization lengths. The scan #0 analysis is used to estimate uncertainties and baseline levels of the gray level residuals. All subsequent scans #1 through #6 have comparable residuals; the DVC analyses were deemed successful. Figure 10(b) displays the equilibrium gap Φ_m as a function of the root mean square (RMS) gray level residual Φ_c for the maximum prescribed displacement (*i.e.,* scan # 6). As expected, the higher the weight given to the penalty term, directly dependent on the regularization length, the lower the equilibrium gap Φ_m. At the same time, the gray level residual increases with the regularization length. To pick the best trade-off between equilibrium gap and gray level residuals, the so-called L-curve criterion [44] was utilized. It consists in looking for the maximum curvature in the plot of Figure 10(b). The selected regularization length was then $\ell_m = 25$ vx (Table 4).

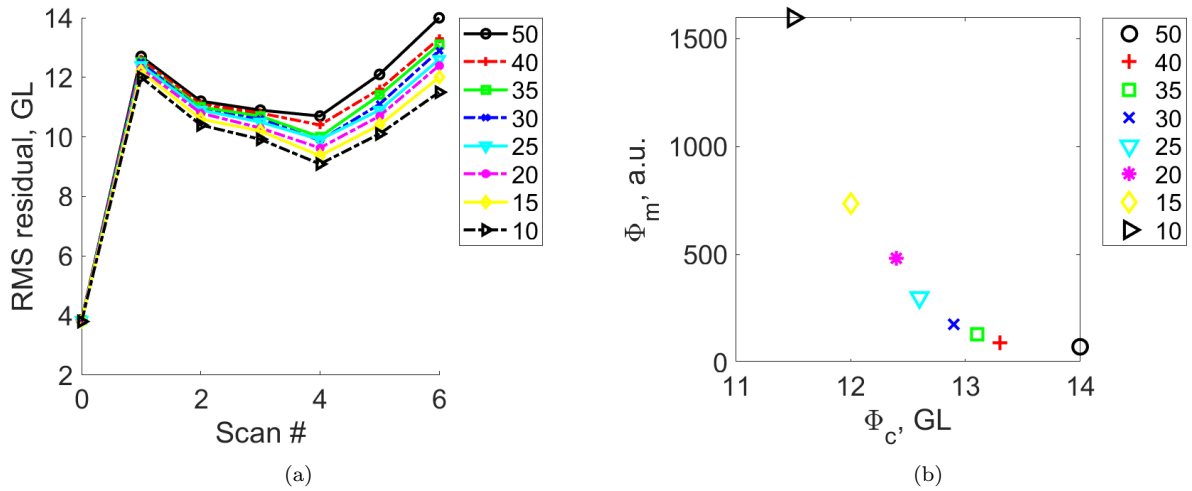

(a) (b)

Figure 10: (a) RMS gray level residual Φ_c for the seven acquired scans compared with the reference one for different regularization lengths (expressed in voxels). (b) RMS gray level residual Φ_c vs. equilibrium gap Φ_m for 28 mm stroke.

4.3.3 Measured displacement fields

The DVC analysis allowed the displacement fields to be measured for all scans in the loaded configurations. Figures 11-13 show the measured components of the displacement field in the vertical, longitudinal and transverse directions, respectively, for the last loading step (*i.e.,* 28 mm stroke). The displacement amplitudes were very large compared to the overall dimensions of the specimen. As a consequence of the prescribed displacement in the vertical direction, the specimen shortened significantly in that direction, except for the ends due to the constrained shafts, which translated almost rigidly. One may notice that the measured vertical displacement is within a range significantly larger than the prescribed displacement, which for the last loading step corresponds to about 240 voxels (Figures 11). While the bottom of the specimen remained essentially flat, the shafts at the left and right ends had a different behavior, which explains the different measured ranges. At the ends of the specimen, the deformation of the extreme cylinders, which are forced out of horizontal placement and come closer to each other (*i.e.,* the bottom shaft inflects upward and the top shaft does so downward). Thus, the maximum vertical displacement is measured in the middle of the lower ending shafts, where the prescribed displacement is summed to a further positive one due to flexure.

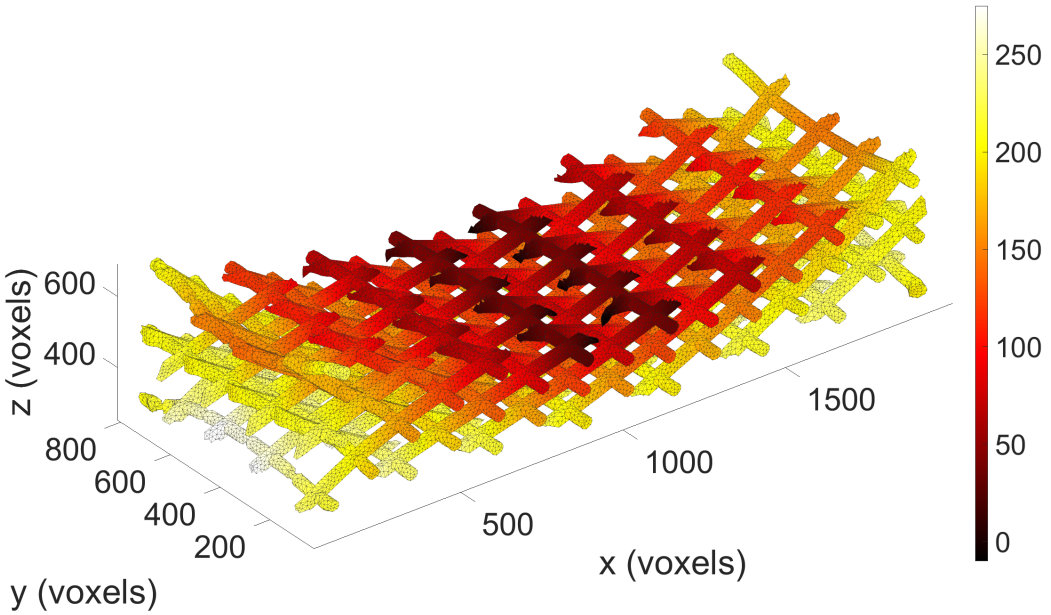

Figure 11: Vertical displacement field on the mesh in its deformed configuration for 28 mm deflection. Labels are expressed in voxels.

As a consequence of the pantographic structure, prescribing a vertical flexural displacement, the effect on the specimen is to produce also very significant motions in the longitudinal direction (Figures 12). The range of measured longitudinal displacement is $[-140, 175]$ voxels, corresponding to an overall elongation of the sample of 36.4 mm (*i.e.,* about 20% of its initial length).

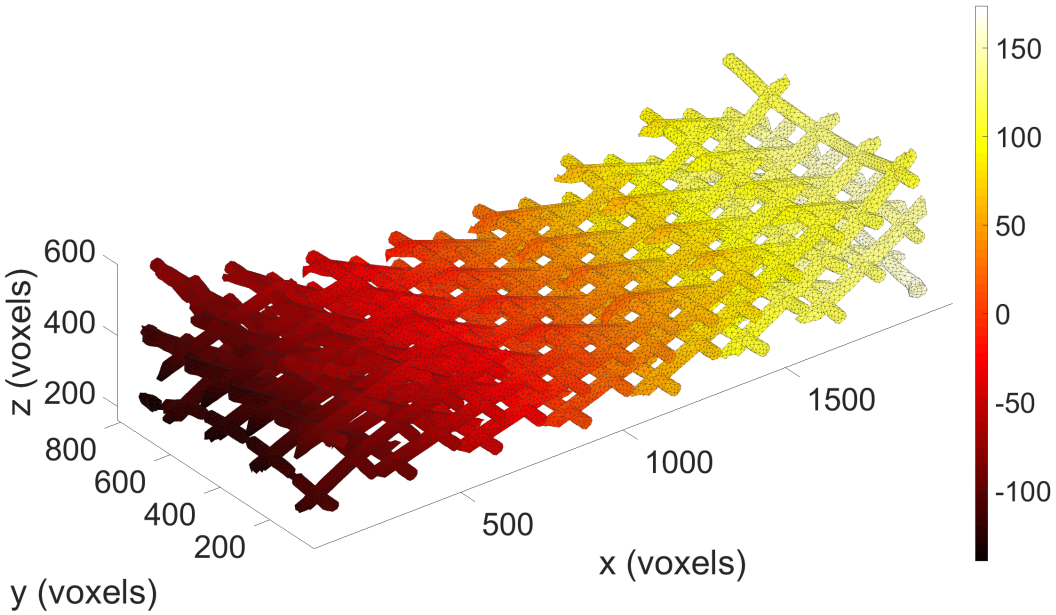

Figure 12: Longitudinal displacement field on the mesh in its deformed configuration for 28 mm deflection. Labels are expressed in voxels.

Shear of the vertical transverse cross-sections at the ends of the sample is also observed when looking at the measured transverse displacement (Figures 13). This deformation results in a slight twist of the sample. The same behaviour can already be observed in the bi-dimensional case [33]. Note that the direction of twist is not random but due to the chirality of the specimen (moving in the longitudinal direction, one meets orthogonally 4 planes of ascending beams and 4 with descending beams, and reversing them results in a chiral specimen, which would have twisted in the other direction).

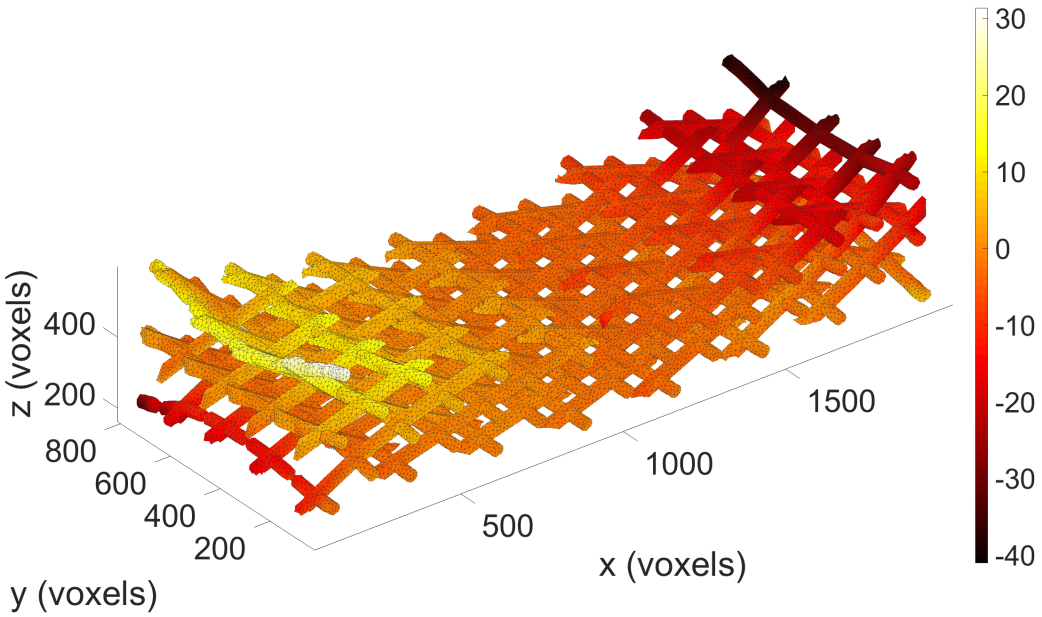

Figure 13: Transverse displacement field on the mesh in its deformed configuration for 28 mm deflection. Labels are expressed in voxels.

4.4 Numerical simulations

Numerical simulations of the three-point flexural test were conducted using the identical setup as in the previous experiment. The model described in Section 3 was implemented within COMSOL Multiphysics using the weak formulation tool that allows the elastic energy in Eq. (2) and Eq. (5) to be given. The beams added to the system to impede the floppy modes were modeled by considering a further energetic contribution encoded in the four short sides parallel to the vertical direction of the continuous parallelepiped describing the pantographic block where they were attached. The expression of this energy density per unit line in terms of displacement $\boldsymbol{u}$ of the four considered edges is assumed to be

$$W_r = \frac{1}{2}\mathrm{K}_r\left(\sqrt{(u_{1,3})^2+(u_{2,3})^2+(1+u_{3,3})^2}-1\right)^2+\frac{1}{2}\mathrm{K}_{b1}(u_{1,33})^2+\frac{1}{2}\mathrm{K}_{b2}(u_{2,33})^2 \tag{12}$$

where three main contributions are considered, namely, the first one is related to the change in the length of the beams, and the other two take into account the flexural behavior in the xy- and yz-planes, respectively. The stretching contribution is a nonlinear term, while, for the sake of simplicity, the flexural contributions were linearized. The corresponding stiffnesses K_r, K_{b1} and K_{b2} were evaluated from the beam theory and their values were $\mathrm{K}_r = 18007$ N, $\mathrm{K}_{b1} = 0.1$ Nm^2, and $\mathrm{K}_{b2} = 0.02$ Nm^2.

The numerical simulations were performed using 85,931 tetrahedral elements, corresponding to 734,991 degrees of freedom. Since second-gradient contributions are present in Eq. (2), Hermite-type shape functions

of cubic order were selected. This choice satisfies the minimum requirement for approximating the space of solutions, which is a Hilbert space H^2 for this case.

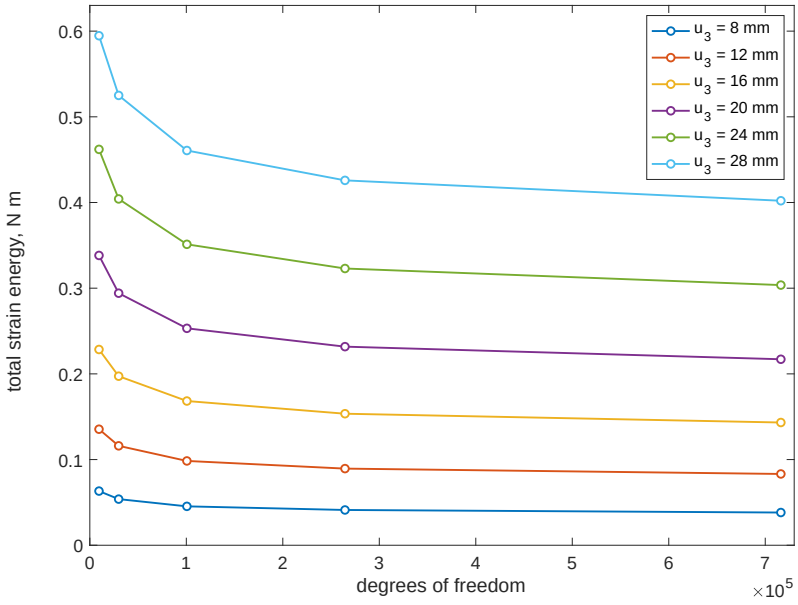

Figure 14: Convergence plots.

Figure 14 shows the plot of convergence of the total strain energy versus the number of degrees of freedom in the examined three-point flexural test for different values of prescribed displacement. It is important to note that the convergence analysis presented herein is not intended toward a known limit solution since it is almost impossible to obtain a closed-form solution as a benchmark for the problem at hand. However, a closed-form solution was not needed since one can directly compare the numerical results with the measurements to have an idea of how good the simulations are. The analysis shows that the numerical solutions obtained by decreasing the mesh size (i.e., increasing the number of degrees of freedom) are characterized by the fact that the difference between any two solutions can be made arbitrarily small if the difference between the largest mesh size between the two solutions is small enough.

During the considered test, the supports interact with the sample block. This interaction was accounted for using a quadratic elastic potential barrier. This barrier prevents the sample from interpenetrating the support, whose shape was assumed to be cylindrical. A frictionless penalty method was considered to model contact between the supports and the sample. Such an interaction is modeled with an infinite distribution of springs surrounding the supports and the loading pin of the testing machine. This distribution of springs is activated only when the rigid shape of the supports and the loading pin attempt to penetrate the specimen by applying a repulsive force. The specimen was placed on the motionless lower supports. The third loading support was then used to gradually deform the specimen by moving it downward.

The results of the finite element simulations are illustrated in Figures 15-17. In the plots, the black

material lines are drawn on the side of the specimen only for readability purposes to illustrate the predicted beam deformation. A qualitative agreement with the experimental results is observed.

In Figure 15, we plot the vertical displacement numerically forecast. As it happened for the analogous measurement illustrated in Figure 11, a shift in the overall range can be observed, resulting in a maximum vertical displacement of about 7 mm instead of 0. Again, this is due to the bending of the edges parallel to the $\{y\}$ direction that results in a positive displacement in the bottom of the sample.

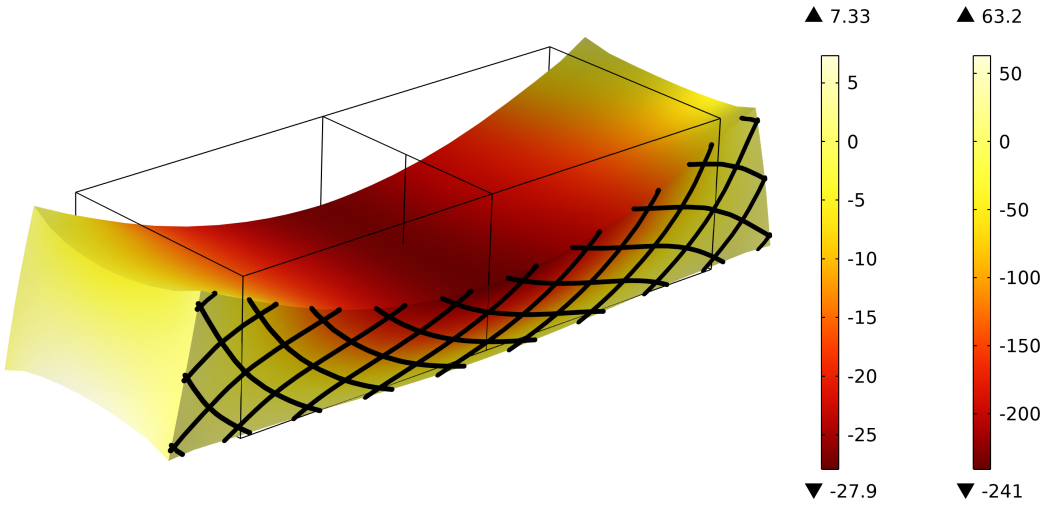

Figure 15: Vertical displacement field on the continuum sample for 28 mm deflections. Labels are expressed in mm (left color bar) and in voxels (right color bar).

Figure 16 illustrates the numerical prediction of the longitudinal displacements. The behavior is mainly governed by the pantographic mechanism that produces significant elongations of the overall sample as a response to the external excitation.

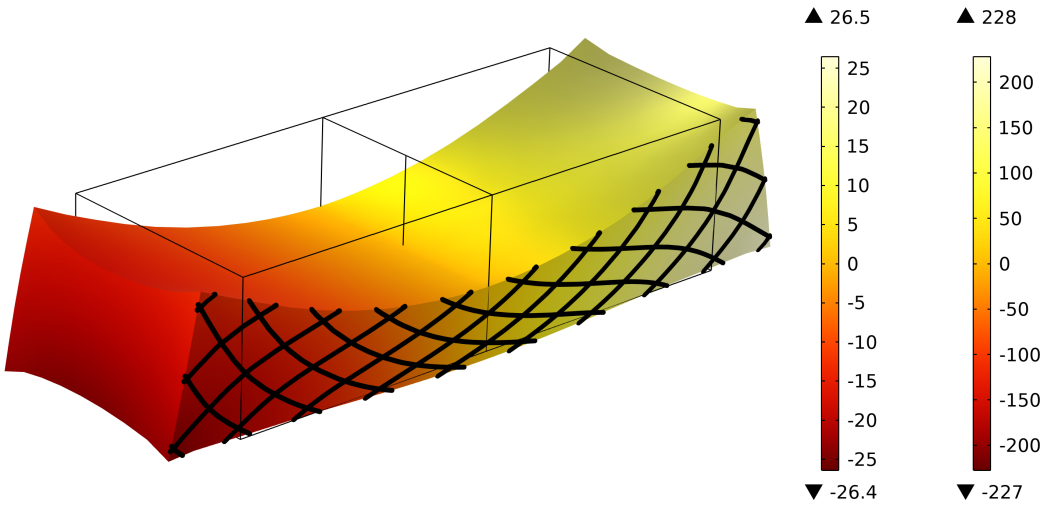

Figure 16: Longitudinal displacement field on the continuum sample for 28 mm deflections. Labels are expressed in mm (left color bar) and in voxels (right color bar).

In Figure 17, the transverse displacement is displayed. The sample twist due to chirality and the presence of clearances are not captured as these features were not taken into account in the numerical model. Small transverse displacements are observed in the regions close to the sample ends where the elastic lockings were placed.

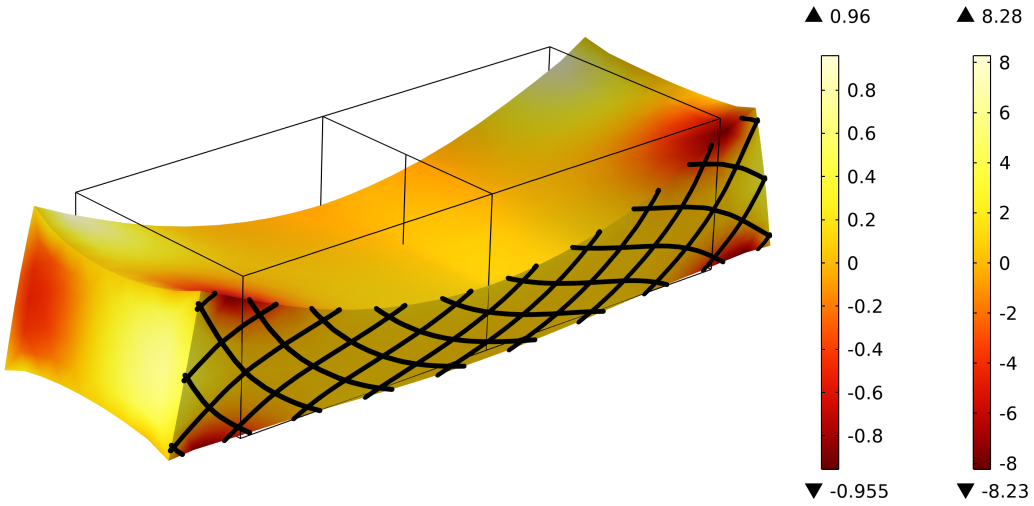

Figure 17: Transverse displacement field on the continuum sample for 28 mm deflections. Labels are expressed in mm (left color bar) and in voxels (right color bar).

A quantitative comparison between the experimental and numerical results is proposed in the following. In the continuum model, the focus is on the material points occupying at rest the position of the centers of the hinges. The numerical prediction of the placement of these points in the loaded configuration is compared

with the current position of the centers of the hinges in the experiment. Figure 18 shows the side view of the specimen for the 28 mm prescribed deflection and the numerical prediction of the placement of the centers of the hinges illustrated by the colored circles. It is observed that the numerical prediction, besides its good qualitative agreement, is not quantitatively fully accurate. The predicted longitudinal displacement is larger than the experimental one. In the vertical direction, the agreement is not perfect either.

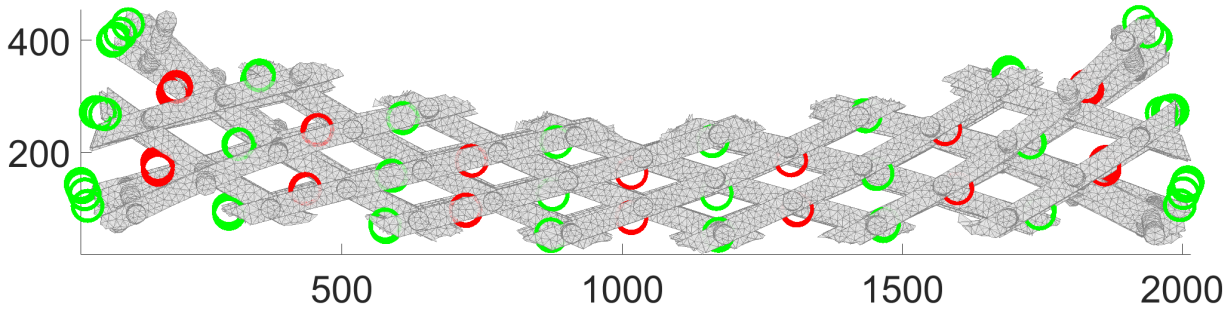

Figure 18: Numerical prediction of the positions of the centers of the hinges (circles) over the experimental deformed shape of the specimen for 28 mm imposed deflection. The green circles refer to the vertical rows with three hinges, while the red circles correspond to the rows with two hinges. The labels are expressed in voxels.

These quantitative issues seem to be related to the particular characteristics of the designed geometry, which make it difficult for the continuum model to fully capture the behavior. In particular, the clearances in the hinges were not modeled in the continuum case and become relevant, especially in the longitudinal direction, where a cumulative effect is visible. These clearances, combined with the chirality of the specimen, also make the object prone to transverse deflection. Thus, the description of a low-density designed pantographic specimen with a continuum model, although quite robust (see also in a bi-dimensional case [64]), most likely introduced additional sources of discrepancies.

Last, to illustrate the shield capabilities of the considered metamaterial, the total elastic energy density is displayed for the maximum deformation. Figure 19 illustrates the fact that the energy density (and consequently the inner stress) is spread throughout the entire sample due to the external excitation. However, it mainly concentrated at the ends of the specimen, where four constraints were in place to prevent the floppy modes. Conversely, at the center of the sample, on the opposite side to the application of the external force, a sharp drop in energy of about three orders of magnitude with respect to its maximum level is observed.

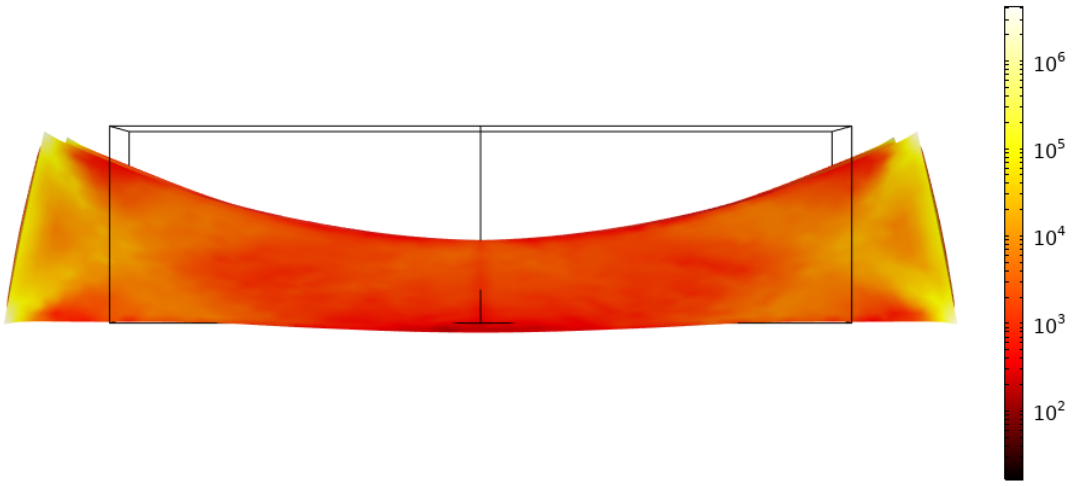

Figure 19: Numerical evaluation of the energy density under the 28 mm prescribed deflection.

5 Conclusions

Pantographic blocks are metamaterials with peculiar mechanical properties, especially when their hinges are perfect. They are made up of a stack of layers, each of which is a pantographic sheet. In the present case, the pantographic block was printed using the Powder Bed Fusion technology, and its hinges were modeled as 'perfect,' namely, rotating joints.

An *in situ* flexural test was performed during which tomographic scans were acquired. They were used to measure displacement fields (via DVC) for different levels of deformation. In the present case, the displacement amplitudes were very high between two consecutive scans, which required the DVC analyses to be carefully initialized. It was shown that the registration results in faithful displacement levels up to 250 voxels.

The predictions of a second gradient model for the mechanical response of the pantographic block were checked experimentally. The pantographic block almost entirely shielded the deformation applied by the upper support. The mechanical model explains this mechanism in terms of an "arching" effect activated in the beams constituting the pantographic structure and the elastic deformation in the side structural elements introduced for locking floppy modes. The presented experimental evidence shows that the concept that inspired the pantographic block design was well-grounded.

It is worth noting that the mechanical behavior of the studied metamaterial is mainly due to the peculiar pantographic architecture and is almost independent of the material (see, e.g., Refs. [16, 72] where the pantographic sheet behaved in the same qualitative way even though the material was a polymer or a metal). The share of different contributions of energy can be easily controlled if one thinks that the primary stored energy in the constitutive elements is related to the change in length of the beams as well as their bending.

With the same material, the area of the beam cross-section influences the extension of the beams, while the moment of inertia influences their flexural deformation. By changing the geometry of the cross-section, it is possible to tailor the energy ratio between these two contributions. The shear deformation in the pantographic plane is very small, while the shear deformation in the other two orthogonal planes is small (and does not introduce any exotic behavior). This last energy contribution is mainly related to how the joints are made.

Using the methods presented in Refs. [22, 31], it is expected that an optimization procedure may be established, which will determine the best distribution of elastic and perfect hinges in the structure to minimize the block lower face displacement, possibly delaying failure. As future development, it is interesting to note that the evolution of the 3D-printing technology will allow one to fabricate structures having characteristic sizes for pantographic cells of a few micrometers (see, for instance, Refs. [21, 73]), so that applications of such mechanical shield may be considered in a wide range of scenarios.

Although short and long-term inelastic deformations may have a significant impact on the functionality of polymers, this aspect of the behavior was not investigated herein. In future developments, various rheological models will be probed to understand the impact of these deformations on the metamaterial response.

Acknowledgment

This work has been financially supported by the French "Agence Nationale de la Recherche" through the "Investissements d'avenir" program (ANR-10-EQPX-37 MATMECA Grant). This work was carried out under the auspices of the Gruppo Nazionale di Fisica Matematica (GNFM) of the Istituto Nazionale di Alta Matematica (INDAM).

References

[1] B. E. Abali. Revealing the physical insight of a length-scale parameter in metamaterials by exploiting the variational formulation. *Continuum Mechanics and Thermodynamics*, 31(4):885–894, 2019.

[2] B. E. Abali and E. Barchiesi. Additive manufacturing introduced substructure and computational determination of metamaterials parameters by means of the asymptotic homogenization. *Continuum Mechanics and Thermodynamics*, 33(4):993–1009, 2021.

[3] B. E. Abali, B. Vazic, and P. Newell. Influence of microstructure on size effect for metamaterials applied in composite structures. *Mechanics Research Communications*, 122:103877, 2022.

[4] J.-J. Alibert, P. Seppecher, and F. dell'Isola. Truss modular beams with deformation energy depending on higher displacement gradients. *Mathematics and Mechanics of Solids*, 8(1):51–73, 2003.

[5] P. Auger, T. Lavigne, B. Smaniotto, M. Spagnuolo, F. dell'Isola, and F. Hild. Poynting Effects in Pantographic Metamaterial Captured via Multiscale DVC. *Journal of Strain Analysis for Engineering Design*, 56(7):462–477, 2021.

[6] G. Aydin, M.E. Yildizdag, and B.E. Abali. Strain-gradient modeling and computation of 3-d printed metamaterials for verifying constitutive parameters determined by asymptotic homogenization. In *Theoretical Analyses, Computations, and Experiments of Multiscale Materials*, pages 343–357. Springer, 2022.

[7] E. Barchiesi, F. dell'Isola, and F. Hild. On the validation of homogenized modeling for bi-pantographic metamaterials via digital image correlation. *International Journal of Solids and Structures*, 208:49–62, 2021.

[8] E. Barchiesi, Simon R Eugster, F. dell'Isola, and F. Hild. Large in-plane elastic deformations of bi-pantographic fabrics: asymptotic homogenization and experimental validation. *Mathematics and Mechanics of Solids*, 25(3):739–767, 2020.

[9] E. Barchiesi, G. Ganzosch, C. Liebold, L. Placidi, R. Grygoruk, and W.H. Müller. Out-of-plane buckling of pantographic fabrics in displacement-controlled shear tests: experimental results and model validation. *Continuum Mechanics and Thermodynamics*, 31:33–45, 2019.

[10] E. Barchiesi, M. Spagnuolo, and L. Placidi. Mechanical metamaterials: a state of the art. *Mathematics and Mechanics of Solids*, 24(1):212–234, 2019.

[11] Zongqi Bi, Quanmei Gong, Peijun Guo, and Qian Cheng. Experimental study of the evolution of soil arching effect under cyclic loading based on trapdoor test and particle image velocimetry. *Canadian Geotechnical Journal*, 57(6):903–920, 2020.

[12] A. Ciallella, G. La Valle, A. Vintache, B. Smaniotto, and F. Hild. Deformation mode in 3-point flexure on pantographic block. *International Journal of Solids and Structures*, 265:112129, 2023.

[13] M. Cuomo, C. Boutin, L. Contrafatto, and S. Gazzo. Effective anisotropic properties of fibre network sheets. *European Journal of Mechanics-A/Solids*, 93:104492, 2022.

[14] R. Darleux, B. Lossouarn, I. Giorgio, F. dell'Isola, and J.-F. Deü. Electrical analogs of curved beams and application to piezoelectric network damping. *Mathematics and Mechanics of Solids*, 27(4):578–601, 2022.

[15] M. De Angelo, L. Placidi, N. Nejadsadeghi, and A. Misra. Non-standard Timoshenko beam model for chiral metamaterial: identification of stiffness parameters. *Mechanics Research Communications*, 103:103462, 2020.

[16] M. De Angelo, M. Spagnuolo, F. D'Annibale, A. Pfaff, K. Hoschke, A. Misra, C. Dupuy, P. Peyre, J. Dirrenberger, and M. Pawlikowski. The macroscopic behavior of pantographic sheets depends mainly on their microstructure: experimental evidence and qualitative analysis of damage in metallic specimens. *Continuum Mechanics and Thermodynamics*, 31:1181–1203, 2019.

[17] F. dell'Isola, I. Giorgio, M. Pawlikowski, and N.L. Rizzi. Large deformations of planar extensible beams and pantographic lattices: heuristic homogenization, experimental and numerical examples of equilibrium. *Proceedings of the Royal Society A: Mathematical, Physical and Engineering Sciences*, 472(2185):20150790, 2016.

[18] F. dell'Isola, T. Lekszycki, M. Pawlikowski, R. Grygoruk, and L. Greco. Designing a light fabric metamaterial being highly macroscopically tough under directional extension: first experimental evidence. *Zeitschrift für angewandte Mathematik und Physik*, 66:3473–3498, 2015.

[19] F. dell'Isola, P. Seppecher, J.-J. Alibert, T. Lekszycki, R. Grygoruk, M. Pawlikowski, D. Steigmann, I. Giorgio, U. Andreaus, E. Turco, M. Golaszewski, N. Rizzi, C. Boutin, V.A. Eremeyev, A. Misra, L. Placidi, E. Barchiesi, L. Greco, M. Cuomo, A. Cazzani, A.D. Corte, A. Battista, D. Scerrato, I. Zurba Eremeeva, Y. Rahali, J.-F. Ganghoffer, W. Müller, G. Ganzosch, M. Spagnuolo, A. Pfaff, K. Barcz, K. Hoschke, J. Neggers, and F. Hild. Pantographic metamaterials: an example of mathematically driven design and of its technological challenges. *Continuum Mechanics and Thermodynamics*, 31(4):851–884, 2019.

[20] F. dell'Isola, P. Seppecher, M. Spagnuolo, E. Barchiesi, F. Hild, T. Lekszycki, I. Giorgio, L. Placidi, U. Andreaus, M. Cuomo, S.R. Eugster, A. Pfaff, K. Hoschke, R. Langkemper, E. Turco, R. Sarikaya, A. Misra, M. De Angelo, F. D'Annibale, A. Bouterf, X. Pinelli, A. Misra, B. Desmorat, M. Pawlikowski, C. Dupuy, D. Scerrato, P. Peyre, M. Laudato, L. Manzari, P. Göransson, C. Hesch, S. Hesch, P. Franciosi, J. Dirrenberger, F. Maurin, Z. Vangelatos, C. Grigoropoulos, V. Melissinaki, M. Farsari, W. Muller, E. Abali, C. Liebold, G. Ganzosch, P. Harrison, R. Drobnicki, L.A. Igumnov, F. Alzahrani, and T. Hayat. Advances in Pantographic Structures: Design, Manufacturing, Models, Experiments and Image Analyses. *Continuum Mechanics and Thermodynamics*, 31(4):1231–1282, 2019.

[21] F. dell'Isola, E. Turco, A. Misra, Z. Vangelatos, C. Grigoropoulos, V. Melissinaki, and M. Farsari. Force–displacement relationship in micro-metric pantographs: experiments and numerical simulations. *Comptes Rendus Mécanique*, 347(5):397–405, 2019.

[22] B. Desmorat, M. Spagnuolo, and E. Turco. Stiffness optimization in nonlinear pantographic structures. *Mathematics and Mechanics of Solids*, 25(12):2252–2262, 2020.

[23] V. A Eremeyev, F. dell'Isola, C. Boutin, and D. Steigmann. Linear pantographic sheets: existence and uniqueness of weak solutions. *Journal of Elasticity*, 132(2):175–196, 2018.

[24] V.A. Eremeyev, S. A Lurie, Y.O. Solyaev, and F. dell'Isola. On the well posedness of static boundary value problem within the linear dilatational strain gradient elasticity. *Zeitschrift für angewandte Mathematik und Physik*, 71:1–16, 2020.

[25] N. Fang, D. Xi, J. Xu, M. Ambati, W. Srituravanich, C. Sun, and X. Zhang. Ultrasonic metamaterials with negative modulus. *Nature materials*, 5(6):452–456, 2006.

[26] G. Flamourakis, I. Spanos, Z. Vangelatos, P. Manganas, L. Papadimitriou, C. Grigoropoulos, A. Ranella, and M. Farsari. Laser-made 3d auxetic metamaterial scaffolds for tissue engineering applications. *Macromolecular Materials and Engineering*, 305(7):2000238, 2020.

[27] B. Florijn, C. Coulais, and M. van Hecke. Programmable mechanical metamaterials. *Physical review letters*, 113(17):175503, 2014.

[28] S. Gazzo, M. Cuomo, C. Boutin, and L. Contrafatto. Directional properties of fibre network materials evaluated by means of discrete homogenization. *European Journal of Mechanics-A/Solids*, 82:104009, 2020.

[29] Aref Ghorbani, David Dykstra, Corentin Coulais, Daniel Bonn, Erik van der Linden, and Mehdi Habibi. Inverted and programmable Poynting effects in metamaterials. *Advanced Science*, 8(20):2102279, 2021.

[30] I. Giorgio. A discrete formulation of Kirchhoff rods in large-motion dynamics. *Mathematics and Mechanics of Solids*, 25(5):1081–1100, 2020.

[31] I. Giorgio. Lattice shells composed of two families of curved Kirchhoff rods: an archetypal example, topology optimization of a cycloidal metamaterial. *Continuum Mechanics and Thermodynamics*, 33(4):1063–1082, 2021.

[32] I. Giorgio, F. dell'Isola, and D. J. Steigmann. Second-grade elasticity of three-dimensional pantographic lattices: theory and numerical experiments. *Continuum Mechanics and Thermodynamics*, 2023.

[33] I. Giorgio, N.L. Rizzi, U. Andreaus, and D.J. Steigmann. A two-dimensional continuum model of pantographic sheets moving in a 3d space and accounting for the offset and relative rotations of the fibers. *Mathematics and Mechanics of Complex Systems*, 7(4):311–325, 2019.

[34] I. Giorgio, N.L. Rizzi, and E. Turco. Continuum modelling of pantographic sheets for out-of-plane bifurcation and vibrational analysis. *Proceedings of the Royal Society A: Mathematical, Physical and Engineering Sciences*, 473(2207):20170636, 2017.

[35] I. Giorgio and D. Scerrato. Multi-scale concrete model with rate-dependent internal friction. *European Journal of Environmental and Civil Engineering*, 21(7-8):821–839, 2017.

[36] M. Golaszewski, R. Grygoruk, I. Giorgio, M. Laudato, and F. Di Cosmo. Metamaterials with relative displacements in their microstructure: technological challenges in 3D printing, experiments and numerical predictions. *Continuum Mechanics and Thermodynamics*, 31:1015–1034, 2019.

[37] L. Greco. An iso-parametric G^1-conforming finite element for the nonlinear analysis of Kirchhoff rod. Part I: the 2D case. *Continuum Mechanics and Thermodynamics*, 32(5):1473–1496, 2020.

[38] L. Greco, M. Cuomo, D. Castello, and A. Scrofani. An updated lagrangian bézier finite element formulation for the analysis of slender beams. *Mathematics and Mechanics of Solids*, 27(10):2110–2138, 2022.

[39] E. F. Grekova, A. V. Porubov, and F. dell'Isola. Reduced linear constrained elastic and viscoelastic homogeneous cosserat media as acoustic metamaterials. *Symmetry*, 12(4):521, 2020.

[40] A. Grillo, S. Federico, and G. Wittum. Growth, mass transfer, and remodeling in fiber-reinforced, multi-constituent materials. *International Journal of Non-Linear Mechanics*, 47(2):388–401, 2012.

[41] R.J. Guyan. Reduction of stiffness and mass matrices. *AIAA Journal*, 3(2):380–380, 1965.

[42] Dong Han, Xin Ren, Chen Luo, Yi Zhang, Xiang Yu Zhang, Xue Gang Zhang, Wei Jiang, Jian Hao, and Yi Min Xie. Experimental and computational investigations of novel 3D printed square tubular lattice metamaterials with negative Poisson's ratio. *Additive Manufacturing*, 55:102789, 2022.

[43] Dong Han, Xin Ren, Yi Zhang, Xiang Yu Zhang, Xue Gang Zhang, Chen Luo, and Yi Min Xie. Lightweight auxetic metamaterials: Design and characteristic study. *Composite Structures*, 293:115706, 2022.

[44] P.C. Hansen. The L-Curve and its Use in the Numerical Treatment of Inverse Problems. In *in Computational Inverse Problems in Electrocardiology, ed. P. Johnston, Advances in Computational Bioengineering*, pages 119–142. WIT Press, 2000.

[45] F. Hild, A. Bouterf, L. Chamoin, F. Mathieu, J. Neggers, F. Pled, Z. Tomičević, and S. Roux. Toward 4D Mechanical Correlation. *Advanced Modeling and Simulation in Engineering Sciences*, 3(1):1–26, 2016.

[46] K. Kappe, J. P. Wahl, F. Gutmann, S. M. Boyadzhieva, K. Hoschke, and S. CL Fischer. Design and manufacturing of a metal-based mechanical metamaterial with tunable damping properties. *Materials*, 15(16):5644, 2022.

[47] G. La Valle, A. Ciallella, and G. Falsone. The effect of local random defects on the response of pantographic sheets. *Mathematics and Mechanics of Solids*, 27(10):2147–2169, 2022.

[48] B Ladanyi and BJCGJ Hoyaux. A study of the trap-door problem in a granular mass. *Canadian Geotechnical Journal*, 6(1):1–14, 1969.

[49] H. Leclerc, J. Neggers, F. Mathieu, F. Hild, and S. Roux. *Correli 3.0*. IDDN.FR.001.520008.000.S.P.2015.000.31500, Agence pour la Protection des Programmes, Paris (France), 2015.

[50] Nan Li, Wei Zhao, Fengfeng Li, Liwu Liu, Yanju Liu, and Jinsong Leng. A 4D-printed programmable soft network with fractal design and adjustable hydrophobic performance. *Matter*, 6(3):940–962, 2023.

[51] Cheng Lin, Zhipeng Huang, Qinglong Wang, Zhichen Zou, Wenbo Wang, Liwu Liu, Yanju Liu, and Jinsong Leng. Mass-producible near-body temperature-triggered 4D printed shape memory biocomposites and their application in biomimetic intestinal stents. *Composites Part B: Engineering*, 256:110623, 2023.

[52] A. Madeo, P. Neff, I.-D. Ghiba, L. Placidi, and G. Rosi. Wave propagation in relaxed micromorphic continua: modeling metamaterials with frequency band-gaps. *Continuum Mechanics and Thermodynamics*, 27:551–570, 2015.

[53] E. Maire and P. J. Withers. Quantitative X-ray tomography. *International Materials Reviews*, 59(1):1–43, 2014.

[54] J. W. McNulty. *An experimental study of arching in sand*. Number 1. University of Illinois at Urbana-Champaign, 1965.

[55] L. Mizzi, E.M. Mahdi, K. Titov, R. Gatt, D. Attard, K. E Evans, J. N. Grima, and J.-C. Tan. Mechanical metamaterials with star-shaped pores exhibiting negative and zero poisson's ratio. *Materials & Design*, 146:28–37, 2018.

[56] N Nejadsadeghi, M De Angelo, R Drobnicki, T Lekszycki, F Dell'Isola, and A Misra. Parametric experimentation on pantographic unit cells reveals local extremum configuration. *Experimental Mechanics*, 59:927–939, 2019.

[57] N. Nejadsadeghi, L. Placidi, M. Romeo, and A. Misra. Frequency band gaps in dielectric granular metamaterials modulated by electric field. *Mechanics Research Communications*, 95:96–103, 2019.

[58] G S Pardo and E Sáez. Experimental and numerical study of arching soil effect in coarse sand. *Computers and Geotechnics*, 57:75–84, 2014.

[59] S. Patil and B. Ravi. Voxel-based representation, display and thickness analysis of intricate shapes. In *Ninth International Conference on Computer Aided Design and Computer Graphics (CAD-CG'05)*, pages 6 pp.–, 2005.

[60] A. Ramírez-Torres, R. Penta, R. Rodríguez-Ramos, A. Grillo, L. Preziosi, J. Merodio, R. Guinovart-Díaz, and J. Bravo-Castillero. Homogenized out-of-plane shear response of three-scale fiber-reinforced composites. *Computing and Visualization in Science*, 20:85–93, 2019.

[61] S. Roux, F. Hild, P. Viot, and D. Bernard. Three dimensional image correlation from X-Ray computed tomography of solid foam. *Composites Part A: Applied Science and Manufacturing*, 39(8):1253–1265, 2008.

[62] D. Scerrato, I. Giorgio, and N.L. Rizzi. Three-dimensional instabilities of pantographic sheets with parabolic lattices: numerical investigations. *Zeitschrift für angewandte Mathematik und Physik*, 67:1–19, 2016.

[63] P. Seppecher, J.-J. Alibert, and F. dell'Isola. Linear elastic trusses leading to continua with exotic mechanical interactions. In *Journal of Physics: Conference Series*, page 012018. IOP Publishing, 2011.

[64] M. Spagnuolo, M. E. Yildizdag, U. Andreaus, and A. M. Cazzani. Are higher-gradient models also capable of predicting mechanical behavior in the case of wide-knit pantographic structures? *Mathematics and Mechanics of Solids*, 26(1):18–29, 2021.

[65] M. Stilz, F. dell'Isola, I. Giorgio, V.A. Eremeyev, G. Ganzenmüller, and S. Hiermaier. Continuum models for pantographic blocks with second gradient energies which are incomplete. *Mechanics Research Communications*, page 103988, 2022.

[66] M. Stilz, S. R. Eugster, J. Harsch, F. Gutmann, G. Ganzenmüller, and S. Hiermaier. A second-gradient elasticity model and isogeometric analysis for the pantographic ortho-block. *International Journal of Solids and Structures*, page 112358, 2023.

[67] M. Stilz, D. Plappert, F. Gutmann, and S. Hiermaier. A 3D extension of pantographic geometries to obtain metamaterial with semi-auxetic properties. *Mathematics and Mechanics of Solids*, 27(4):673–686, 2022.

[68] T. Taillandier-Thomas, S. Roux, T.F. Morgeneyer, and F. Hild. Localized strain field measurement on laminography data with mechanical regularization. *Nuclear Instruments and Methods in Physics Research Section B*, 324:70–79, 2014.

[69] E. Turco, E. Barchiesi, and F. dell'Isola. Nonlinear dynamics of origami metamaterials: energetic discrete approach accounting for bending and in-plane deformation of facets. *Zeitschrift für angewandte Mathematik und Physik*, 74(1):26, 2023.

[70] E. Turco, K. Barcz, M. Pawlikowski, and N.L. Rizzi. Non-standard coupled extensional and bending bias tests for planar pantographic lattices. part i: numerical simulations. *Zeitschrift für angewandte Mathematik und Physik*, 67:1–16, 2016.

[71] E. Turco, F. Dell'Isola, N.L. Rizzi, Roman Grygoruk, Wolfgang H Müller, and Christian Liebold. Fiber rupture in sheared planar pantographic sheets: numerical and experimental evidence. *Mechanics Research Communications*, 76:86–90, 2016.

[72] E. Turco, A. Misra, M. Pawlikowski, F. dell'Isola, and F. Hild. Enhanced Piola–Hencky discrete models for pantographic sheets with pivots without deformation energy: numerics and experiments. *International Journal of Solids and Structures*, 147:94–109, 2018.

[73] Z. Vangelatos, M. E. Yildizdag, I. Giorgio, F. dell'Isola, and C. Grigoropoulos. Investigating the mechanical response of microscale pantographic structures fabricated by multiphoton lithography. *Extreme Mechanics Letters*, 43:101202, 2021.

[74] F. Wang, M. Brøns, and O. Sigmund. Non-hierarchical architected materials with extreme stiffness and strength. *Advanced Functional Materials*, 33(13):2211561, 2023.

Appendix: DVC hardware and DVC parameters

Table 3 reports the hardware parameters of the experiment, and Table 4 the DVC parameters.

Table 3: DVC hardware parameters

Tomograph	North Star Imaging X50+
X-ray source	XRayWorX XWT-240-CT
Target / Anode	W (reflection mode)
Filter	none
Voltage	150 kV
Current	600 µA
Tube to detector	943.537 mm
Tube to object	727.347 mm
Detector	Dexela 2923
Definition	1536 × 1944 pixels (2 × 2 binning)
Number of projections	1200
Angular amplitude	360°
Frame average	5 per projection
Frame rate	13 fps
Acquisition duration	23 min 56 s
Reconstruction algorithm	filtered back-projection
Gray Levels amplitude	8 bits
Volume size	2069 × 856 × 649 voxels (after crop)
Field of view	240.0 × 99.3 × 74.9 mm^3 (after crop)
Image scale	116 µm/voxel

Table 4: DVC analysis parameters

DIC software	Correli 3.0 [49]
Image filtering	none
Element length (mean)	6 vx
Shape functions	linear (T4 elements [45])
Mesh	see Figure 7
Matching criterion	penalized sum of squared differences
Regularization length	$\ell_m = 25$ vx
Interpolant	cubic